MIT Libraries | DSpace@MIT

MIT Open Access Articles

Weyl Semimetal Phase in Noncentrosymmetric Transition-Metal Monophosphides

The MIT Faculty has made this article openly available. ***Please share*** how this access benefits you. Your story matters.

Citation: Weng, Hongming et al. "Weyl Semimetal Phase in Noncentrosymmetric Transition-Metal Monophosphides." Physical Review X 5.1 (March 2015)

As Published: http://dx.doi.org/10.1103/PhysRevX.5.011029

Publisher: American Physical Society

Persistent URL: http://hdl.handle.net/1721.1/96148

Version: Final published version: final published article, as it appeared in a journal, conference proceedings, or other formally published context

Terms of use: Creative Commons Attribution

Massachusetts Institute of Technology

Weyl Semimetal Phase in Noncentrosymmetric Transition-Metal Monophosphides

Hongming Weng,[1,2,*] Chen Fang,[3] Zhong Fang,[1,2] B. Andrei Bernevig,[4] and Xi Dai[1,2]

[1]*Beijing National Laboratory for Condensed Matter Physics, and Institute of Physics, Chinese Academy of Sciences, Beijing 100190, China*

[2]*Collaborative Innovation Center of Quantum Matter, Beijing 100084, China*

[3]*Department of Physics, Massachusetts Institute of Technology, Cambridge, Massachusetts 02139, USA*

[4]*Department of Physics, Princeton University, Princeton, New Jersey 08544, USA*

(Received 12 January 2015; published 17 March 2015)

Based on first-principle calculations, we show that a family of nonmagnetic materials including TaAs, TaP, NbAs, and NbP are Weyl semimetals (WSM) without inversion centers. We find twelve pairs of Weyl points in the whole Brillouin zone (BZ) for each of them. In the absence of spin-orbit coupling (SOC), band inversions in mirror-invariant planes lead to gapless nodal rings in the energy-momentum dispersion. The strong SOC in these materials then opens full gaps in the mirror planes, generating nonzero mirror Chern numbers and Weyl points off the mirror planes. The resulting surface-state Fermi arc structures on both (001) and (100) surfaces are also obtained, and they show interesting shapes, pointing to fascinating playgrounds for future experimental studies.

DOI: 10.1103/PhysRevX.5.011029

Subject Areas: Condensed Matter Physics, Materials Science, Topological Insulators

I. INTRODUCTION

Most topological invariants in condensed-matter noninteracting phases are defined on closed manifolds in momentum space. For gapped systems, both the Chern insulator and Z_2 topological insulator phases can be defined using the Berry phase and curvature in either the entire or half of the two-dimensional (2D) Brillouin zone (BZ), respectively [1,2]. A similar idea can be generalized to gapless metallic systems. In three-dimensional (3D) systems, besides the BZ, an important closed manifold in momentum space is a 2D Fermi surface (FS). Topological metals can be defined by Chern numbers of the single-particle wave functions at the Fermi surface energies [3–5]. Such nonzero FS Chern numbers appear when the FS encloses a band-crossing point—the Weyl point—which can be viewed as a singular point of Berry curvature or "magnetic monopole" in momentum space [6–9]. Materials with such Weyl points near the Fermi level are called Weyl semimetals (WSM) [7–10].

Weyl points can only appear when the spin-doublet degeneracy of the bands is removed by breaking either time reversal T or spacial inversion symmetry P (in fact, Weyl points exist if the system does not respect $T \cdot P$). In these cases, the low-energy single-particle Hamiltonian around a Weyl point can be written as a 2×2 "Weyl equation," which is half of the Dirac equation in three dimensions. According to the "no-go theorem" [11,12], for any lattice model, the Weyl points always appear in pairs of opposite chirality or monopole charge. The conservation of chirality is one of the many ways to understand the topological stability of the WSM against any perturbation that preserves translational symmetry: The only way to annihilate a pair of Weyl points with opposite chirality is to move them to the same point in BZ. Since generically the Weyls can sit far away from each other in the BZ, this requires large changes of Hamiltonian parameters, and the WSM is stable. The existence of Weyl points near the Fermi level will lead to several unique physical properties, including the appearance of discontinuous Fermi surfaces (Fermi arcs) on the surface [7–9], the Adler-Bell-Jackiw anomaly [10,13–15], and others [16,17].

The first proposal to realize WSM in condensed-matter materials was suggested in Ref. [7] for $Rn_2Ir_2O_7$ pyrochlore with all-in/all-out magnetic structure, where 24 pairs of Weyl points emerge as the system undergoes the magnetic ordering transition. A relatively simpler system $HgCr_2Se_4$ [9] was then proposed by some of the present authors, where a pair of double-Weyl points due to quadratic band crossing appear when the system is in a ferromagnetic phase. Another proposal involves a fine-tuned multilayer structure of normal insulators and magnetically doped topological insulators [18]. These proposed WSM systems involve magnetic materials, where the spin degeneracy of the bands is removed by breaking time-reversal symmetry. As mentioned, the WSM can also be

*hmweng@iphy.ac.cn

Published by the American Physical Society under the terms of the Creative Commons Attribution 3.0 License. Further distribution of this work must maintain attribution to the author(s) and the published article's title, journal citation, and DOI.

generated by breaking the spatial inversion symmetry only, a method which has the following advantages. First, compared with magnetic materials, nonmagnetic WSM are much more easily studied experimentally using angle-resolved photo emission spectroscopy (ARPES) as alignment of magnetic domains is no longer required. Second, without the spin exchange field, the unique structure of Berry curvature leads to very unusual transport properties under a strong magnetic field, unspoiled by the magnetism of the sample.

Currently, there are several representative proposals for WSM generated by inversion symmetry breaking. The first one is a superlattice system formed by alternatively stacking normal and topological insulators [19,20]. The second one involves tellurium or selenium crystals under pressure [21]. The third one is the solid solutions of $A\mathrm{Bi}_{1-x}\mathrm{Sb}_x\mathrm{Te}_3$ (A = La and Lu) [22] and $\mathrm{TlBi}(\mathrm{S}_{1-x}R_x)_2$ (R = Se or Te) [23] tuned around the topological transition points [24]. The fourth one is a model based on zinc-blende structure [25] with the fine-tuning of the relative strength between SOC and the inversion symmetry-breaking term. But none of the above proposals has been realized experimentally. In the present study, we predict that TaAs, TaP, NbAs, and NbP single crystals are natural WSM, and each of them possesses a total of 12 pairs of Weyl points. Compared with the existing proposals, this family of materials is completely stoichiometric and, therefore, are easier to grow and measure. Unlike in the case of pyrochlore iridates and $HgCr_2Se_4$, where inversion is still a good symmetry and the appearance of Weyl points can be immediately inferred from the product of the parities at all the time-reversal invariant momenta (TRIM) [26–28], in the TaAs, family parity is no longer a good quantum number. However, the appearance of Weyl points can still be inferred by analyzing the mirror Chern numbers (MCN) [29,30] and Z_2 indices [26,31] for the four mirror and time-reversal invariant planes in the BZ. Similar to many other topological materials, the WSM phase in this family is also induced by a type of band-inversion phenomena, which, in the absence of spin-orbit coupling (SOC), leads to nodal rings in the mirror plane. Once the SOC is turned on, each nodal ring will be gapped with the exception of three pairs of Weyl points leading to fascinating physical properties which include complicated Fermi arc structures on the surfaces.

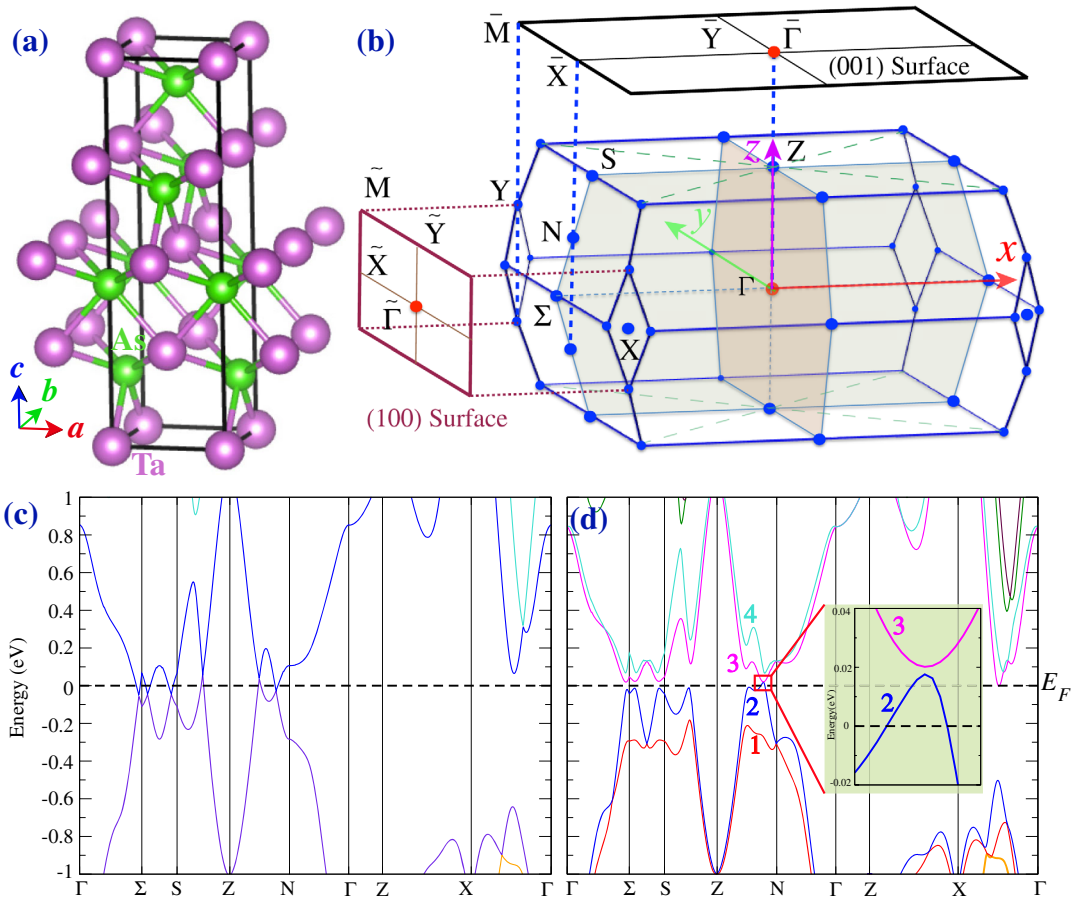

FIG. 1. Crystal structure and Brillouin zone (BZ). (a) The crystal symmetry of TaAs. (b) The bulk BZ and the projected surface BZ for both (001) and (100) surfaces. (c) The band structure of TaAs calculated by GGA without including the spin-orbit coupling. (d) The band structure of TaAs calculated by GGA with the spin-orbit coupling.

II. CRYSTAL STRUCTURE AND CALCULATION METHODS

As all four mentioned materials share very similar band structures, in the rest of the paper, we will choose TaAs as the representative material to introduce the electronic structures of the whole family. The experimental crystal structure of TaAs [32] is shown in Fig. 1(a). It crystalizes in body-centered-tetragonal structure with nonsymmorphic space group $I4_1md$ (No. 109), which lacks inversion symmetry. The measured lattice constants are $a = b =$ 3.4348 Å and $c = 11.641$ Å. Both Ta and As are at $4a$ Wyckoff position (0, 0, u) with $u = 0$ and 0.417 for Ta and As, respectively. We have employed the software package OpenMX [33] for the first-principles calculation. It is based on norm-conserving pseudopotential and pseudo-atomic localized basis functions. The choice of pseudopotentials, pseudo-atomic orbital basis sets (Ta9.0-s2p2d2f1 and As9.0-s2p2d1), and the sampling of BZ with a $10 \times 10 \times 10$ grid have been carefully checked. The exchange-correlation functional within a generalized gradient approximation (GGA) parametrized by Perdew, Burke, and Ernzerhof has been used [34]. After full structural relaxation, we obtain the lattice constants $a = b =$ 3.4824 Å, $c = 11.8038$ Å and optimized $u = 0.4176$ for the As site, in very good agreement with the experimental values. To calculate the topological invariant such as MCN and surface states of TaAs, we have generated atomiclike Wannier functions for Ta $5d$ and As $4p$ orbitals using the scheme described in Ref. [35].

III. RESULTS

A. Band structures with and without spin-orbit coupling

We first obtain the band structure of TaAs without SOC by GGA and plot it along the high-symmetry directions in Fig. 1(c). We find clear band inversion and multiple band crossing features near the Fermi level along the ZN, ZS, and ΣS lines. The space group of the TaAs family contains two mirror planes, namely, M_x and M_y [shaded planes in Fig. 1(b)] and two glide mirror planes, namely, M_{xy} and M_{-xy} [illustrated by the dashed lines in Fig. 1(b)]. The plane spanned by Z, N, and Γ points is invariant under mirror M_y, and the energy bands within the plane can be labeled by mirror eigenvalues ± 1. Further symmetry analysis shows that the two bands that cross along the Z to N line belong to opposite mirror eigenvalues, and hence, the crossing between them is protected by mirror symmetry. Similar band crossings can also be found along other high-symmetry lines in the ZNΓ plane, i.e., the ZS and NS lines. Altogether, these band crossing points form a "nodal ring" in the ZNΓ plane as shown in Fig. 2(b). Unlike for the situation in the ZNΓ plane, in the two glide mirror planes (M_{xy} and M_{-xy}), the band structure is fully gapped, with a minimum gap of roughly 0.5 eV.

The analysis of orbital character shows that the bands near the Fermi energy are mainly formed by Ta $5d$ orbitals, which have large SOC. Including SOC in the first-principle calculation leads to a dramatic change of the band structure near the Fermi level, as plotted in Fig. 1(d). At first glance, it seems that the previous band crossings in the ZNΓ plane are all gapped, with the exception of one point along the ZN line. Detailed symmetry analysis reveals that the bands "2" and "3" in Fig. 1(d) belong to opposite mirror eigenvalues, indicating the almost-touching point along the ZN line is completely accidental. In fact, there is a small gap of roughly 3 meV between bands "2" and "3" as illustrated by the inset of Fig. 1(d). The ZNΓ plane then becomes fully gapped once SOC is turned on.

B. Topological invariants for mirror plane and Weyl points

Since the material has no inversion center, the usual parity condition [26–28] cannot be applied to predict the existence of WSM. We then resort to another strategy. As previously mentioned, the space group of the material provides two mirror planes (M_x and M_y), where the MCN can be defined. If a full gap exists for the entire BZ, the MCN would directly reveal whether this system is a topological crystalline insulator or not. Interestingly, as shown below, if the system is not fully gapped, we can still use the MCN to find out whether the material hosts Weyl points in the BZ or not. Besides the two mirror planes, we have two additional glide mirror planes (M_{xy} and M_{-xy}). Although the MCN is not well defined for the glide mirror planes, the Z_2 index is still well defined here as these planes are time-reversal invariant. We then apply the Wilson-loop method to calculate the MCNs for the two mirror planes and Z_2 indices for the two glide mirror planes. Here, we just briefly describe the essence of this method. For a more detailed explanation of the method, please refer to Refs. [5,37]. A Wilson loop is an arbitrary closed k-point loop in BZ, evaluated around which, the occupied Bloch functions acquire a total Berry phase $\theta(w)$, with w being the loop index. One can define a series of parallel Wilson loops w to fully cover a closed 2D manifold in 3D momentum space, such as a cut plane in BZ or a closed FS as stated in the beginning of this paper. Then, the evolution of $\theta(w)$ along these parallel Wilson loops (it turns out to be a 1D problem) gives information on the band-structure topology on the closed 2D manifold. For example, to determine the MCNs for the mirror plane M_x, we define Wilson loops along the k_x direction with fixed k_z. All the occupied bands at k points in this plane can be classified into two groups according to their eigenvalues under mirror operation, i or $-i$. Taking those having eigenvalue i, the evolution of Berry phases along the periodic k_z direction can be obtained, and the MCN is simply its winding number.

The results are plotted in Fig. 2(d), which shows that MCN is 1 for the ZNΓ plane (M_y) and the Z_2 index is even or trivial for the ZXΓ plane (M_{xy}). Then, if we consider the (001) surface, which is invariant under the M_y mirror. The nontrivial helical surface modes will appear because of the nonzero MCN in the ZNΓ plane, which generates a single pair of FS cuts along the projective line of the ZNΓ plane [the x axis in Fig. 2(c)]. Whether these Fermi cuts will eventually form a single closed Fermi circle or not depends on the Z_2 index for the two glide mirror planes, which are projected to the dashed blue lines in Fig. 2(c). Since the Z_2 indices for the glide mirror planes are trivial, as confirmed by our Wilson-loop calculation plotted in Fig. 2(d), there are no protected helical edge modes along the projective lines of the glide mirror planes [dashed blue lines in Fig. 2(c)], and the Fermi cuts along the x axis in Fig. 2(c) must end somewhere between the x axis and the diagonal lines [dashed blue lines in Fig. 2(c)]. In other words, they must be Fermi arcs, indicating the existence of Weyl points in the bulk band structure of TaAs.

From the above analysis of the MCN and Z_2 index of several high-symmetry planes, we can conclude that Weyl points exist in the TaAs band structure. We now determine the total number of Weyl points and their exact positions. This is a hard task, as the Weyl points are located at generic k points without any little-group symmetry. For this purpose, we calculate the integral of the Berry curvature on a closed surface in k space, which equals the total chirality of the Weyl points enclosed by the given surface. Because of the fourfold rotational symmetry and mirror planes that characterize TaAs, we only need to search for the Weyl points within the reduced BZ—one-eighth of the whole BZ. We first calculate the total chirality or monopole charge enclosed in the reduced BZ. The result is 1, which guarantees the existence of, and odd number of, Weyl points. To determine precisely the location of each Weyl point, we divide the reduced BZ into a very dense k-point mesh and compute the Berry curvature or the "magnetic field in momentum space" [35,38] on that mesh, as shown in Fig. 3. From this, we can easily identify the precise

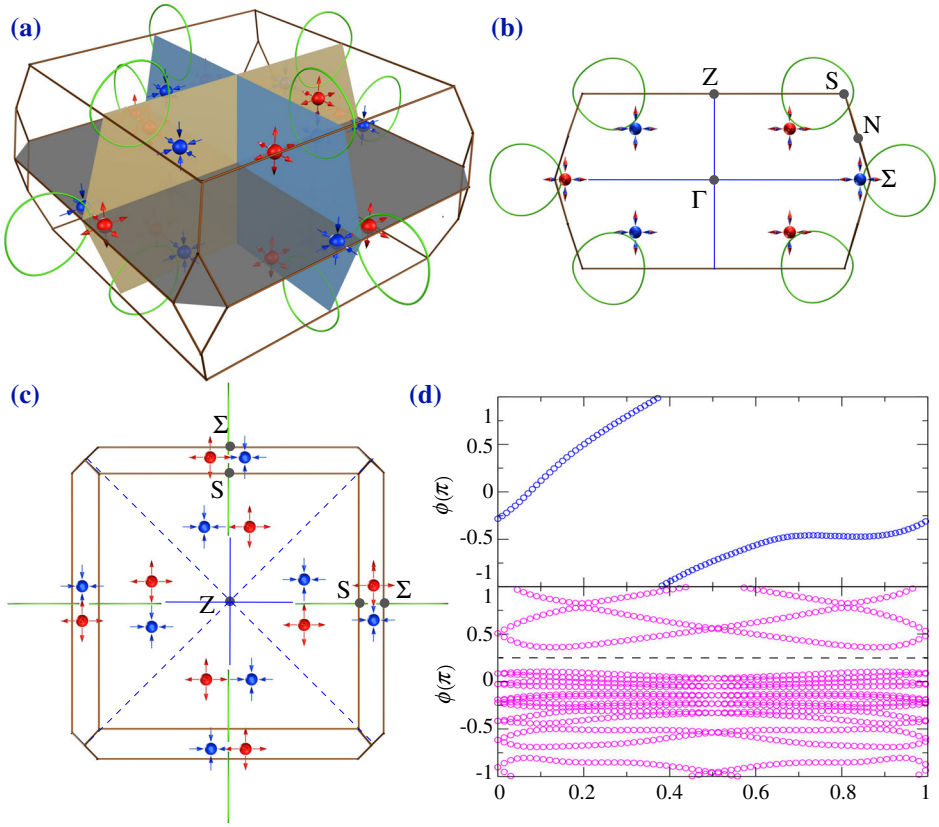

FIG. 2. Nodal rings and Weyl points distribution, as well as Z_2 and MCN for mirror planes. (a) 3D view of the nodal rings (in the absence of SOC) and Weyl points (with SOC) in the BZ. (b) Side view from [100] and (c) top view from [001] directions for the nodal rings and Weyl points. Once the SOC is turned on, the nodal rings are gapped and give rise to Weyl points off the mirror planes (see movie in Supplemental Material [36]). (d) Top panel: Flow chart of the average position of the Wannier centers obtained by Wilson-loop calculation for bands with mirror eigenvalue i in the mirror plane ZNΓ. (d) Bottom panel: The flow chart of the Wannier centers obtained by Wilson-loop calculation for bands in the glide mirror plane ZXΓ. There is no crossing along the reference line (the dashed line), indicating the Z_2 index is even.

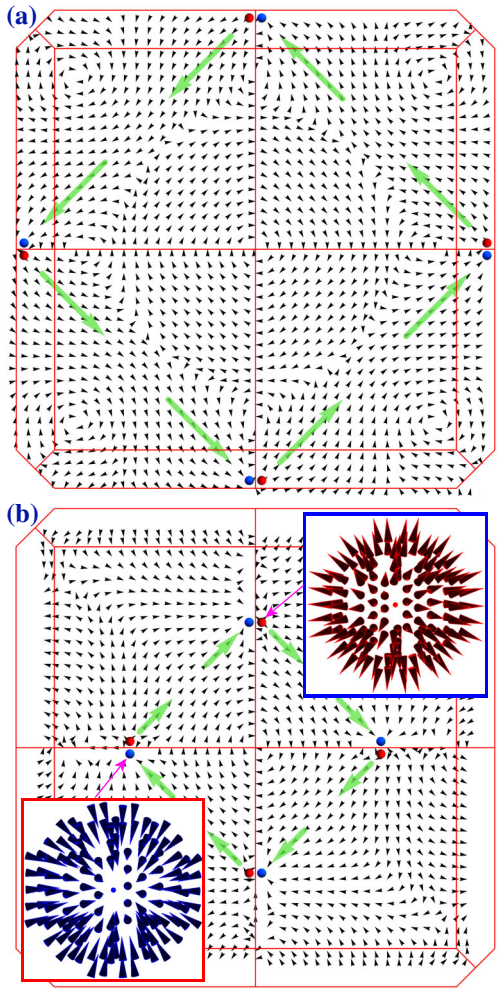

FIG. 3. Berry curvature from pairs of Weyl points. (a) The distribution of the Berry curvature for the $k_z = 0$ plane, where the blue and red dots denote the Weyl points with chirality of $+1$ and -1, respectively; (b) same as (a) but for the $k_z = 0.592\pi$ plane. The insets show the 3D view of hedgehoglike Berry curvature near the two selected Weyl points.

position of the Weyl points by searching for the "source" and "drain" points of the "magnetic field." The Weyl points in TaAs are illustrated in Fig. 2(a), where we find 12 pairs of Weyl points in the vicinity of what used to be, in the SOC-free case, the nodal rings on two of the mirror-invariant planes. For each of the mirror-invariant planes, after turning on SOC, the nodal rings will be fully gapped within the plane, but isolated gapless nodes slightly off plane appear, as illustrated in Fig. 2(b). Two pairs of Weyl points are located exactly in the $k_z = 0$ plane, and another four pairs of Weyl points are located off the $k_z = 0$ plane. Considering the fourfold rotational symmetry, it is then easy to understand that there are a total of 12 pairs of Weyl points in the whole BZ. The Weyl points in the $k_z = 0$ plane are about 2 meV above the Fermi energy and form eight tiny hole pockets, while the others are about 21 meV below the Fermi level to form 16 electron pockets. The appearance of Weyl points can also be derived from a $k \cdot p$ model with different types of mass terms induced by SOC, which will be introduced in detail in the Appendix. The band structures for the other three materials—TaP, NbAs, and NbP—are very similar. The precise positions of the Weyl points for all these materials are summarized in Table. I.

TABLE I. The two nonequivalent Weyl points in the xyz coordinates shown in Fig. 1(b). The position is given in units of the length of Γ-Σ for x and y and of the length of Γ-Z for z.

	Weyl node 1	Weyl node 2
TaAs	(0.949, 0.014, 0.0)	(0.520, 0.037, 0.592)
TaP	(0.955, 0.025, 0.0)	(0.499, 0.045, 0.578)
NbAs	(0.894, 0.007, 0.0)	(0.510, 0.011, 0.593)
NbP	(0.914, 0.006, 0.0)	(0.494, 0.010, 0.579)

C. Fermi arcs and surface states

Unique surface states with unconnected Fermi arcs can be found on the surface of a WSM. These can be understood in the following way: For any surface of a WSM, we can consider small cylinders in the momentum space parallel to the surface normal. In the 3D BZ, these cylinders will be cut by the zone boundary, and their topology is equivalent to that of a closed torus rather than that of open cylinders. If a cylinder encloses a Weyl point, by Stokes theorem, the total integral of the Berry curvature (Chern number) of this closed torus must equal the total "monopole charge" carried by the Weyl point(s) enclosed inside. On the surface of the material, such a cylinder will be projected to a cycle surrounding the projection point of the Weyl point, and a single Fermi surface cut stemming from the chiral edge model of the 2D manifold with Chern number 1 (or -1) must be found on that circle. By varying the radius of the cylinder, it is easy to show that such FSs must start and end at the projection of two (or more) Weyl points with different "monopole charge"; i.e., they must be "Fermi arcs" [7,9,16]. In the TaAs materials family, on most of the common surfaces, multiple Weyl points will be projected on top of each other, and we must generalize the above argument to multiple projections of Weyl points. It is easy to prove that the total number of surface modes at the Fermi level crossing a closed circle in surface BZ must equal the sum of the "monopole charge" of the Weyl points inside the 3D cylinder that projects to the given circle. Another fact controlling the behavior of the surface states is the MCN introduced in the previous discussion, which limits the number of FSs cutting certain projection lines of the mirror plane (when the corresponding mirror symmetries are still preserved on the surface).

By using the Green's function method [5] based on the tight-binding (TB) Hamiltonian generated by the previously obtained Wannier functions, we have computed the

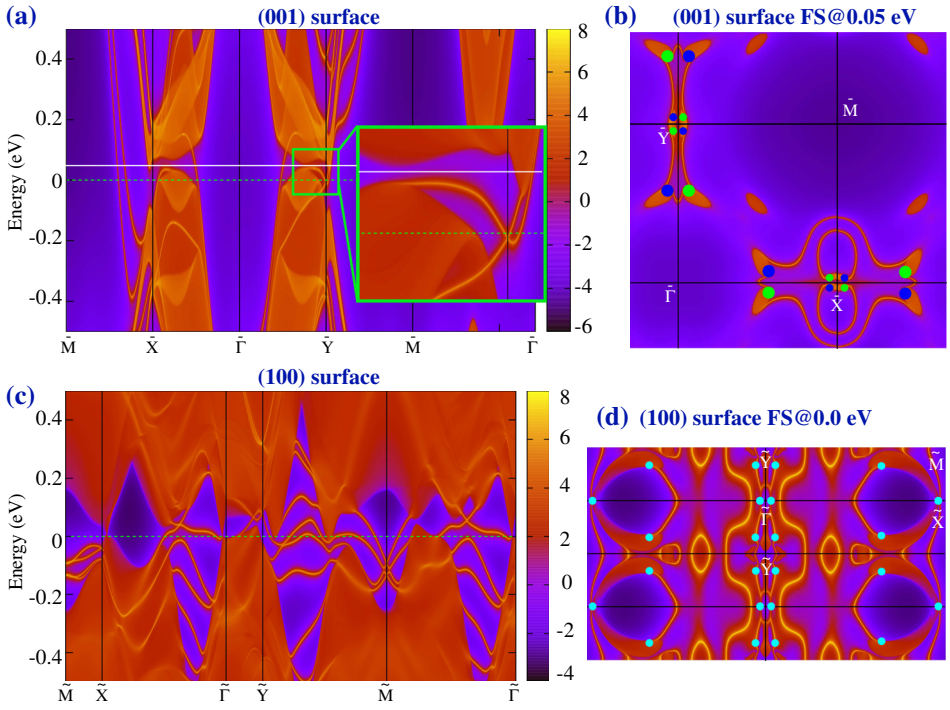

FIG. 4. *Fermi arcs in the surface states.* (a) The Surface states for (001) surface; (b) the corresponding fermi surfaces on (001) surfaces; (c) The Surface states for (100) surface. The dots illustrate the projective points of the bulk Weyl points on the surfaces, where the color represents the chirality of the Weyl points (blue for positive and green for negative), small dot represents the single projected Wely point, and large dot represents two Weyl points with same chirality projecting on top of each other. (d) the corresponding fermi surfaces on (100) surfaces. All the dots here are the projective points for a pair of Weyl points with opposite chirality.

surface states for both (001) and (100) surfaces. They are plotted in Fig. 4 together with the FS plots. On the (001) surface, the crystal symmetry is reduced to C_{2v}, leading to different behavior for the surface bands around the $\bar{X}$ and $\bar{Y}$ points, respectively. Along the $\bar{\Gamma}$-$\bar{X}$ or $\bar{\Gamma}$-$\bar{Y}$ lines, there are two FS cuts with the opposite Fermi velocity satisfying the constraint from the MCN for the ΓZN plane. In addition to the MCN, the possible "connectivity pattern" of the Fermi arcs on the surface has to link different projection points of the Weyl nodes in a way that obeys the chirality condition discussed in the above paragraph. For the (001) surface of TaAs, the connectivity pattern of the Fermi arcs that satisfy all the conditions discussed is not unique. However, due to the fact that all the projective points on the (001) surface are generated either by a single Weyl point or by two Weyl points with the same chirality, the appearance of "Fermi arcs" on the (001) surface is guaranteed. The actual Fermi-arc connectivity pattern for the (001) surface is shown in Fig. 4(b), obtained by our *ab initio* calculation on a nonrelaxed surface described by the TB model. Changes of surface potentials or the simple relaxation of the surface charge density might lead to transitions of the Fermi-arc connectivity pattern and may result in topological Fermi-arc phase transitions on the surface. A very interesting point of the (001) surface states are the extremely long Fermi arcs that cross the zone boundary along the $\bar{X}$ to $\bar{M}$ line. Compared to other proposed WSM materials, the Fermi arcs in TaAs families are much longer, which greatly facilitates their detection in experiments.

Compared to the (001) surface, the (100) surface states of TaAs are much more complicated, as shown in Figs. 4(c) and 4(d). The biggest difference between the (100) and (001) surfaces is that all the projected Weyl points on the (100) surface are formed by a pair of Weyl points with opposite chirality, which does not guarantee (but does not disallow) the existence of the Fermi arcs. The only constraint for the (100) surface states is the nonzero MCN of the ΓZN plane, which generates a pair of chiral modes along the $\bar{\Gamma}$ $\bar{Y}$ line, the projection of the mirror plane, as illustrated in Fig. 4(d).

IV. DISCUSSION

In summary, a family of nonmagnetic WSM materials is proposed in the present paper. Each material in this family contains 12 pairs of Weyl points, which appear because of the lack of an inversion center in the crystal structure and can be derived from the nonzero MCN for two of the mirror-invariant planes in the BZ. The surface states of these materials form quite complicated patterns for the Fermi surfaces, which are determined by both the chirality distribution of the Weyl points and the MCNs for the mirror-invariant planes.

ACKNOWLEDGMENTS

We acknowledge helpful discussions with A. Alexandradinata and N. P. Ong, and thank Rui Yu for help in plotting Fig. 3. This work was supported by the National Natural Science Foundation of China, the 973 program of China (No. 2011CBA00108 and No. 2013CB921700), and the "Strategic Priority Research Program (B)" of the Chinese Academy of Sciences (No. XDB07020100). The calculations were preformed on TianHe-1(A), the National Supercomputer Center in Tianjin, China. B. A. B. acknowledges support from ARO MURI on topological insulators, Grant No. W911NF-12-1-0461, along with NSF CAREER DMR-0952428, ONR-N00014-11-1-0635, and the Packard Foundation.

APPENDIX: $k \cdot p$ MODEL OF A NODAL RING AND THE APPEARANCE OF WEYL POINTS DUE TO SPIN-ORBIT COUPLING

We perform a $k \cdot p$ analysis in the vicinity of the Σ point in the 3D BZ. We show that (1) a nodal ring (a closed line of band-touching points) is protected in the presence of a mirror-reflection symmetry and SU(2) spin-rotation symmetry (when spin-orbit coupling is absent), and (2) when SOC is turned on and all crystalline symmetries are preserved, the nodal ring may be partially gapped with several distinct possibilities: (i) Weyl nodes on the (001) plane, (ii) Weyl nodes away from the (001) plane, and (iii) nodal rings on the (010) plane and (iv) full gap. The realization of these different possibilities strongly depends on the specific form of the SOC terms.

The nodal ring around the Σ point can be modeled by a two-band $k \cdot p$ theory, in the absence of SOC:

$$H_0(\mathbf{k}) = \sum_{i=x,y,z} d_i(\mathbf{k})\sigma_i, \tag{A1}$$

where $d_i(\mathbf{k})$ are real functions and $\mathbf{k} = (k_x, k_y, k_z)$ are three components of the momentum $\mathbf{k}$ relative to the Σ point along [100], [010], and [001] axes, respectively. In Eq. (A1), we have ignored the kinetic term proportional to the identity matrix, as it is irrelevant in studying the band touching. The mirror-reflection symmetry, denoted by M_{010}, is represented by $M = \sigma_z$: In the absence of SOC, we can choose a mirror symmetry that squares to unity. The form of the mirror operator is chosen such that the two bands have opposite mirror eigenvalues, information obtained from the *ab initio* calculation. The mirror reflection dictates that

$$MH_0(k_x, k_y, k_z)M^{-1} = H_0(k_x, -k_y, k_z), \tag{A2}$$

which translates into

$$d_{x,y}(k_x, k_y, k_z) = -d_{x,y}(k_x, -k_y, k_z), \tag{A3}$$

$$d_z(k_x, k_y, k_z) = d_z(k_x, -k_y, k_z). \tag{A4}$$

Equation (A3) states that on the plane $k_y = 0$, only d_z is nonzero, and hence, generically, the equation $d_z(k_x, 0, k_z) = 0$ will have codimension one, i.e., a nodal line solution. Symmetry-preserving perturbations involve gradually changing the forms of the d_i's without violating Eq. (A3), so the nodal ring is robust against them.

Another symmetry is present at the Σ point: a twofold rotation C_2 about the [001] axis followed by time-reversal symmetry. The symmetry is present because the rotation sends the Σ point to its time-reversal partner, and a further time-reversal operation sends it back. This symmetry may be represented by $C_{2T} = U_T K$, where U_T is any symmetric and unitary matrix and K is complex conjugation. Without SOC, the rotation about the [001] axis and the reflection about the (010) plane commute with each other, so we require

$$[\sigma_z, KU_T] = 0, \tag{A5}$$

and we may choose $U_T = \sigma_z$. This symmetry places additional constraints on the d_i's:

$$H_0(k_x, k_y, k_z) = \sigma_z H_0^*(k_x, k_y, -k_z)\sigma_z \tag{A6}$$

or

$$\begin{aligned} d_{y,z}(k_x, k_y, k_z) &= d_{y,z}(k_x, k_y, -k_z), \\ d_x(k_x, k_y, k_z) &= -d_x(k_x, k_y, -k_z). \end{aligned} \tag{A7}$$

Equations (A3) and (A7) determine the general form of our $k \cdot p$ model.

Now we consider adding spin-orbit coupling terms while respecting the symmetries at the Σ point. We first need to determine the matrix representations of the generators of the little group, i.e., M_{010} and $C_2 * T$. Considering spin degrees of freedom, we know that (i) a mirror reflection consists of a spatial reflection and a twofold spin rotation about the axis perpendicular to the reflection plane, (ii) a twofold rotation involves a spatial twofold rotation and a twofold spin rotation about the same axis, and (iii) time-reversal symmetry involves complex conjugation and a flipping of the spin. Following these facts, we obtain the matrix representations

$$\begin{aligned} M &= i\sigma_z \otimes s_y, \\ C_{2T} &= K\sigma_z \otimes s_x. \end{aligned} \tag{A8}$$

Notice that now $M^2 = -1$ and $C_{2T}^2 = 1$, as needed. With spin degrees of freedom, each band in the previous spin-orbit coupling free model in Eq. (A1) becomes two bands, and the nodal ring becomes a four-band crossing. In the vicinity of the nodal ring, the addition of SOC is equivalent

to adding coupling between different spin components, i.e., "mass terms," to the previous model. Here, the name mass term simply means that these terms are not required to vanish at the nodal ring by any symmetry.

The symmetry of the nodal ring is just a mirror reflection. The mass terms hence must commute with mirror symmetry, and a generic term on the $k_y = 0$ plane is given by

$$H_m = m_1(\mathbf{k})s_y + m_2(\mathbf{k})\sigma_z s_y + m_3(\mathbf{k})\sigma_x s_x + m_4(\mathbf{k})\sigma_x s_z + m_5(\mathbf{k})\sigma_y s_z + m_6(\mathbf{k})\sigma_y s_x. \tag{A9}$$

Note that these mass terms are, in general, $\mathbf{k}$ dependent, as their values may change as $\mathbf{k}$ moves along the nodal ring, but the $C_2 * T$ symmetry makes them satisfy (on the $k_y = 0$ plane)

$$m_{1,2,4,6}(k_x, 0, k_z) = m_{1,2,4,6}(k_x, 0, -k_z) = m_{1,2,4,6}(k_x, 0, k_z),$$
$$m_{3,5}(k_x, 0, k_z) = -m_{3,5}(k_x, 0, -k_z) = m_{3,5}(k_x, 0, k_z). \tag{A10}$$

A complete analysis of the band crossing in the presence of all six mass terms is unavailable as the analytic expressions for the dispersion are involved. However, one may see the qualitative role played by each mass term by analyzing them separately. From Eq. (A10), we see that $m_{3,5}$ are odd under $k_z \to -k_z$, while the others are even. This indicates that only $m_{1,2,4,6}$ terms are responsible for band crossings appearing on the $k_z = 0$ plane, while the band crossings away from that plane are attributed mainly to the presence of $m_{3,5}$ terms.

At the $k_y = 0$ plane, $m_{1,2}$ terms commute with H_0, so these terms, if of small strength, will split the doubly degenerate nodal ring into two singly degenerate rings but not open gaps. The equations for the two new rings are given by

$$d_z(k_x, 0, k_z) \pm m_{1,2} = 0. \tag{A11}$$

One should note that when the m_1 term (m_2 term) is added, the two rings are the crossing between two bands with the same (opposite) mirror eigenvalues. Therefore, the two rings from adding the m_1 term are purely accidental, and the two rings from adding the m_2 term are protected by mirror symmetry.

Next, we discuss the effect of the $m_{4,6}$ terms, which should, in combination, give rise to the pair of Weyl nodes on the $k_z = 0$ plane shown in Fig. 2. The dispersion after adding the $m_{4,6}$ terms is

$$E(\mathbf{k}) = \sqrt{d^2 + m_4^2 + m_6^2 \pm 2\sqrt{m_4^2 d_x^2 + m_6^2 d_y^2 + m_4^2 m_6^2}}, \tag{A12}$$

where $d^2 = d_x^2 + d_y^2 + d_z^2$. With some straightforward algebraic work, it can be shown that the equation $E(\mathbf{k}) = 0$ (band touching) is equivalent to the following equations:

$$d_x = d_z = 0,$$
$$d_y^2 = m_6^2 - m_4^2. \tag{A13}$$

When $|m_6| > |m_4|$, these equations have at least one pair of solutions on the $k_z = 0$ plane symmetric about $k_y = 0$ with codimension zero: They are Weyl nodes on the $k_z = 0$ plane. In our simulation, we found only one pair of Weyl nodes appearing on this plane, which can only be understood if $m_{4,6}$ are $\mathbf{k}$ dependent. The equations $d_x = 0$ and $d_z = 0$ determine a closed loop on the $k_z = 0$ plane. At the same time, $d_y(k_x, k_y, 0) = \pm\sqrt{m_6^2 - m_4^2}$ has solutions that are symmetric about $k_y = 0$. Since $d_y(k_x, 0, 0) = 0$, the solutions do not cross the $k_y = 0$ line if $m_{4,6}$ are constants. Therefore, the solutions must be two lines, which make four crossings in total with the solution to $d_z = 0$. However, let us recall that all mass terms can also contain a linear function in k_x, so it is possible that $m_6 - m_4$ vanishes for a particular k_x. At that k_c, the solution to $d_y = \sqrt{m_6^2 - m_4^2} = 0$ is satisfied at $k_y = 0$. If the point $(k_c, 0, 0)$ is inside the loop that solves $d_z(k_x, k_y, 0) = 0$, then there must be an odd number of crossings of $d_y = \sqrt{m_6^2 - m_4^2}$ and $d_z = 0$.

We can also understand the pairs of Weyl nodes that are away from the $k_z = 0$ plane. Consider a coexistence of both m_4 and m_5 terms. The dispersion is given by

$$E(\mathbf{k}) = \sqrt{(d_x \pm m_4)^2 + (d_y \pm m_5)^2 + d_z^2}. \tag{A14}$$

Solving $E(\mathbf{k}) = 0$ is equivalent to solving

$$d_z = 0,$$
$$d_x = \pm m_4,$$
$$d_y = \pm m_5. \tag{A15}$$

The last two equations together give

$$k_z^2 = \sqrt{v m_4/\lambda}, \tag{A16}$$

$$k_y^2 = \sqrt{m_4 \lambda / v}, \tag{A17}$$

where $d_x \equiv u k_y k_z$, $m_5 \equiv \lambda k_z$, and $d_y \equiv v k_y$.

When $v m_4 \lambda < 0$, there is no solution. When $v m_4 \lambda < 0$, there are four sets of solutions for (k_y, k_z). We can substitute them into $d_z = 0$ to obtain the four Weyl nodes observed in our simulation. When m_4 is small, the four Weyl nodes are close to the crossing point of the nodal ring and the $k_z = 0$ plane.

We summarize the roles played by different mass terms: $m_{1,2}$ terms split the nodal ring into two nondegenerate rings. With the m_1 (m_2) term alone, the ring is the crossing of two bands with the same (opposite) mirror eigenvalues. $m_{3,5}$ terms gap the nodal ring except at $k_y = k_z = 0$. The m_4 term alone or coexisting with the m_3 term fully gaps the ring. The m_4 term coexisting with m_5 produces four Weyl nodes away from the $k_z = 0$ plane. The m_6 term creates a pair of Weyl nodes on the $k_z = 0$ plane, symmetric about $k_y = 0$.

[1] M. Z. Hasan and C. L. Kane, *Colloquium: Topological Insulators*, Rev. Mod. Phys. **82**, 3045 (2010).

[2] X. L. Qi and S. C. Zhang, *Topological Insulators and Superconductors*, Rev. Mod. Phys. **83**, 1057 (2011).

[3] Z. Wang, Y. Sun, X.-Q. Chen, C. Franchini, G. Xu, H. Weng, X. Dai, and Z. Fang, *Dirac Semimetal and Topological Phase Transitions in A_3Bi (A = Na, K, Rb)*, Phys. Rev. B **85**, 195320 (2012).

[4] Z. Wang, H. Weng, Q. Wu, X. Dai, and Z. Fang, *Three-Dimensional Dirac Semimetal and Quantum Transport in* Cd_3As_2, Phys. Rev. B **88**, 125427 (2013).

[5] H. Weng, X. Dai, and Z. Fang, *Exploration and Prediction of Topological Electronic Materials Based on First-Principles Calculations*, MRS Bull. **39**, 849 (2014).

[6] Z. Fang, N. Nagaosa, K. S. Takahashi, A. Asamitsu, R. Mathieu, T. Ogasawara, H. Yamada, M. Kawasaki, Y. Tokura, and K. Terakura, *The Anomalous Hall Effect and Magnetic Monopoles in Momentum Space*, Science **302**, 92 (2003).

[7] X. Wan, A. M. Turner, A. Vishwanath, and S. Y. Savrasov, *Topological Semimetal and Fermi-Arc Surface States in the Electronic Structure of Pyrochlore Iridates*, Phys. Rev. B **83**, 205101 (2011).

[8] L. Balents, *Weyl Electrons Kiss*, Physics **4**, 36 (2011).

[9] G. Xu, H. Weng, Z. Wang, X. Dai, and Z. Fang, *Chern Semimetal and the Quantized Anomalous Hall Effect in* $HgCr_2Se_4$, Phys. Rev. Lett. **107**, 186806 (2011).

[10] H. B. Nielsen and M. Ninomiya, *The Adler-Bell-Jackiw Anomaly and Weyl Fermions in a Crystal*, Phys. Lett. B **130**, 389 (1983).

[11] H. B. Nielsen and M. Ninomiya, *Absence of Neutrinos on a Lattice: (I). Proof by Homotopy Theory*, Nucl. Phys. **B185**, 20 (1981).

[12] H. B. Nielsen and M. Ninomiya, *Absence of Neutrinos on a Lattice: (II). Intuitive Topological Proof*, Nucl. Phys. **B193**, 173 (1981).

[13] H.-J. Kim, K.-S. Kim, J.-F. Wang, M. Sasaki, N. Satoh, A. Ohnishi, M. Kitaura, M. Yang, and L. Li, *Dirac Versus Weyl Fermions in Topological Insulators: Adler-Bell-Jackiw Anomaly in Transport Phenomena*, Phys. Rev. Lett. **111**, 246603 (2013).

[14] P. Hosur, S. Parameswaran, and A. Vishwanath, *Charge Transport in Weyl Semimetals*, Phys. Rev. Lett. **108**, 046602 (2012).

[15] S. A. Parameswaran, T. Grover, D. A. Abanin, D. A. Pesin, and A. Vishwanath, *Probing the Chiral Anomaly with Nonlocal Transport in Three-Dimensional Topological Semimetals*, Phys. Rev. X **4**, 031035 (2014).

[16] P. Hosur and X. Qi, *Recent Developments in Transport Phenomena in Weyl Semimetals*, Comp. Rend. Phys. **14**, 857 (2013).

[17] G. E. Volovik, *From Standard Model of Particle Physics to Room-Temperature Superconductivity*, arXiv:1409.3944.

[18] A. A. Burkov and L. Balents, *Weyl Semimetal in a Topological Insulator Multilayer*, Phys. Rev. Lett. **107**, 127205 (2011).

[19] G. B. Halász and L. Balents, *Time-Reversal Invariant Realization of the Weyl Semimetal Phase*, Phys. Rev. B **85**, 035103 (2012).

[20] A. A. Zyuzin, S. Wu, and A. A. Burkov, *Weyl Semimetal with Broken Time Reversal and Inversion Symmetries*, Phys. Rev. B **85**, 165110 (2012); T. Das, *Weyl Semimetal and Superconductor Designed in an Orbital-Selective Superlattice*, Phys. Rev. B **88**, 035444 (2013).

[21] M. Hirayama, R. Okugawa, S. Ishibashi, S. Murakami, and T. Miyake, *Weyl Node and Spin Texture in Trigonal Tellurium and Selenium*, arXiv:1409.7517.

[22] J. Liu and D. Vanderbilt, *Weyl Semimetals from Noncentrosymmetric Topological Insulators*, Phys. Rev. B **90**, 155316 (2014).

[23] B. Singh, A. Sharma, H. Lin, M. Z. Hasan, R. Prasad, and A. Bansil, *Topological Electronic Structure and Weyl Semimetal in the* $TlBiSe_2$ *Class of Semiconductors*, Phys. Rev. B **86**, 115208 (2012).

[24] S. Murakami, *Phase Transition between the Quantum Spin Hall and Insulator Phases in 3D: Emergence of a Topological Gapless Phase*, New J. Phys. **9**, 356 (2007).

[25] T. Ojanen, *Helical Fermi Arcs and Surface States in Time-Reversal Invariant Weyl Semimetals*, Phys. Rev. B **87**, 245112 (2013).

[26] L. Fu, C. Kane, and E. Mele, *Topological Insulators in Three Dimensions*, Phys. Rev. Lett. **98**, 106803 (2007).

[27] A. M. Turner, Y. Zhang, R. S. K. Mong, and A. Vishwanath, *Quantized Response and Topology of Magnetic Insulators with Inversion Symmetry*, Phys. Rev. B **85**, 165120 (2012).

[28] T. L. Hughes, E. Prodan, and B. A. Bernevig, *Inversion-Symmetric Topological Insulators*, Phys. Rev. B **83**, 245132 (2011).

[29] T. H. Hsieh, H. Lin, J. Liu, W. Duan, A. Bansil, and L. Fu, *Topological Crystalline Insulators in the SnTe Material Class*, Nat. Commun. **3**, 982 (2012).

[30] H. Weng, J. Zhao, Z. Wang, Z. Fang, and X. Dai, *Topological Crystalline Kondo Insulator in Mixed Valence Ytterbium Borides*, Phys. Rev. Lett. **112**, 016403 (2014).

[31] C. L. Kane and E. J. Mele, Z_2 *Topological Order and the Quantum Spin Hall Effect*, Phys. Rev. Lett. **95**, 146802 (2005).

[32] S. Furuseth, K. Selte, and A. Kjekshus, *On the Arsenides and Antimonides of Tantalum*, Acta Chem. Scand. **19**, 95 (1965).

[33] See http://www.openmx-square.org.

[34] J. P. Perdew, K. Burke, and M. Ernzerhof, *Generalized Gradient Approximation Made Simple*, Phys. Rev. Lett. **77**, 3865 (1996).

[35] H. Weng, T. Ozaki, and K. Terakura, *Revisiting Magnetic Coupling in Transition-Metal-Benzene Complexes with Maximally Localized Wannier Functions*, Phys. Rev. B **79**, 235118 (2009).

[36] See Supplemental Material at http://link.aps.org/supplemental/10.1103/PhysRevX.5.011029 for a movie demonstrating the distribution of nodal rings and Weyl points in the crystal momentum space.

[37] R. Yu, X. L. Qi, A. Bernevig, Z. Fang, and X. Dai, *Equivalent Expression of $\mathbb{Z}_2$ Topological Invariant for Band Insulators Using the Non-Abelian Berry Connection*, Phys. Rev. B **84**, 075119 (2011).

[38] X. Wang, J. Yates, I. Souza, and D. Vanderbilt, *Ab initio Calculation of the Anomalous Hall Conductivity by Wannier Interpolation*, Phys. Rev. B **74**, 195118 (2006).